

Characterization of Relativistic Electron Precipitation Events Observed by the CALET Experiment Using Self-Organizing-Maps

Sergio. E. Vidal-Luengo¹, Lauren. W. Blum¹, Alessandro Bruno^{2,3}, Anthony W. Ficklin⁴, Georgia de Nolfo², T. Gregory Guzik⁴, Jacob Bortnik⁵, Ryuho Kataoka^{6,7}, Shoji Torii⁸

¹Laboratory of Atmospheric and Space Physics, University of Colorado, Boulder, CO, USA.

²Heliophysics Science Division, NASA Goddard Space Flight Center, Greenbelt, MD, USA

³Department of Physics, Catholic University of America, Washington, DC, USA

⁴Department of Physics and Astronomy, Louisiana State University, Baton Rouge, LA, USA

⁵Department of Atmospheric and Oceanic Sciences, University of California, Los Angeles, CA, USA

⁶National Institute of Polar Research, Tachikawa, Japan

⁷Department of Polar Science, SOKENDAI, Tachikawa, Japan

⁸Waseda Research Institute for Science and Engineering, Waseda University, Shinjuku, Japan

Key Points:

- Relativistic Electron Precipitation (REP) is observed by the CALET experiment from the International Space Station
- The Self-Organizing-Map technique is used for automatic detection and classification of rapidly varying REP intervals
- The Self-Organizing-Maps distinguish between different REP populations

Corresponding author: Sergio E. Vidal-Luengo, Sergio.Vidal-Luengo@lasp.colorado.edu

Abstract

Relativistic electron precipitation (REP) is a relatively high-latitude phenomenon where high-energy electrons trapped in the outer radiation belt are lost into the Earth's atmosphere. REP events observed at low Earth orbit show varying temporal profiles and global distributions. While the precipitation origin has been attributed to specific wave modes or scattering sources, the sorting of REP events by type or driver remains an unsolved challenge. In this study, we analyze the temporal profile of relativistic electron precipitation events observed by the CALorimetric Electron Telescope (CALET) experiment on board the International Space Station. We use an unsupervised machine learning technique called Self-Organizing-Maps (SOM) to automatically detect and then classify relativistic electron events observed by the two scintillator layers at the top of the apparatus, sensitive to electrons with energies > 1.5 MeV and > 3.4 MeV, respectively. We calculate the power spectral density (PSD) of the count rates observed by both sensors and use them as an input for the SOM. The SOM technique groups the PSDs by their similarity, resulting in a classification of relativistic electron events by the periodicity of the observed precipitation. We investigate the L-shell and magnetic local time distribution of the resulting classification, and energy spectral index associated with the observations. Clear precipitation patterns are observed and compared to past precipitation categorization attempts as well as known distributions of various scattering mechanisms. The classification reveals features through the sorting of the variability of the rapid precipitation, allowing the identification of different precipitation populations with varying properties.

Plain Language Summary

Fast electrons are normally trapped by the Earth's magnetic field. However, they often get released in bursts and impact the upper layers of the atmosphere near the poles. The underlying processes are still not well understood and debated. In this study we use an unsupervised artificial intelligence technique called Self-Organizing-Maps (SOM) to automatically detect and classify the observations made by a charged particle detector onboard the International Space Station (ISS). The SOM categorizes the bursts based on their variability and group together observations by their similarity. We compare the categorization with the spatial location of the electron bursts. Clear patterns are observed and compared with past categorizations attempts.

1 Introduction

Relativistic Electron Precipitation (REP) refers to electrons with energies greater than hundreds of keV and initially trapped in the outer Van Allen radiation belt that fall into the upper atmosphere due to pitch angle scattering in the loss cone (Shprits et al., 2006; Loto'Aniu et al., 2006; Millan & Thorne, 2007). This phenomenon represents a source of radiation capable of generating atmospheric heating as well as posing a long term health risk for airline pilots and in both, short and long term for astronauts, especially during extravehicular activities (RA et al., 1995; Dachev, 2018; Ueno et al., 2020; Xu et al., 2021). Currently, the most widely accepted mechanism for REP is pitch angle scattering associated with wave-particle interaction or current sheet scattering (CSS) (Summers & Thorne, 2003; W. Li & Hudson, 2019). The former process occurs as result of the resonance of magnetospheric waves with parallel velocity of counter-streaming energetic electrons (Lorentzen et al., 2001; Millan & Thorne, 2007; Blum, Halford, et al., 2015; Blum & Breneman, 2020). Meanwhile, the latter arises from the violation of the first adiabatic invariant when the Earth's magnetic field curvature radius is comparable to the gyroradius of the electrons. It mainly occurs near the equatorial region of the current sheet, hence the name current sheet scattering (Sergeev & Tsyganenko, 1982; Sergeev et al., 1983; Capannolo et al., 2022). Since both mechanisms can generate large losses of relativistic electrons, they are important for maintaining the equilibrium of the outer Van Allen belt, and efforts continue to be made to obtain direct observations of both scattering mechanisms in the radiation belts and precipitation into the upper atmosphere.

Several direct REP measurements have been conducted by spacecraft and balloons during the last four decades. The Heavy Ion Large Telescope (HILT) experiment from the Solar, Anomalous, and Magnetospheric Particle Explorer (SAMPEX) observed that REP events usually have a latitudinal extension of $2\text{-}3^\circ$, and can persist for several hours (Blake et al., 1996). SAMPEX observations also showed the existence of 10-30 seconds time-scale precipitation bands mostly observed in the dusk-midnight sector and of more rapid variations (~ 100 ms) known as microbursts predominantly observed in the dawn-noon sector (Nakamura et al., 1995; Blake et al., 1996; Bortnik et al., 2006; Blum, Li, & Denton, 2015; Crew et al., 2016; Shumko et al., 2018). These REP events have been categorized based on their location in L-shell and MLT coordinate as well as with their correlation with proton precipitation, and lower energetic electrons. Yahnin et al. (2016)

identified a total of three groups of REP events. The first group corresponds to electrons from the isotropic zone near the trapped limit for electrons. This type of precipitation always occurs in the nightside and is likely result of CSS. They also observed a second and third group from electrons deeper in the trapped zone which suggest they are the result from the interaction with waves. The second group corresponds to relativistic electrons observed simultaneously with lower energetic electrons ($> 30\text{keV}$). These events are observed at all MLTs, with a maximum at the pre-midnight sector, and they are more likely to be related to electrostatic waves near the upper-hybrid-frequency, and plasmaspheric hiss. The third group corresponds to REP events correlated with energetic protons observations, suggesting an interaction with EMIC waves, mostly observed in the dusk and pre-midnight sectors.

Blum et al. (2013) and K. Zhang et al. (2017) used the Colorado Student Space Weather Experiment (CSSWE) cubesat and Balloon Array for Radiation-belt Relativistic Electron Losses (BARREL) to study a total of three different precipitation bands events during 18-19 January 2013. Both studies estimated a net loss of the 0.58-1.63 MeV electrons close to 5% of the total electron content, showing the significance of precipitation bands as nearly 15-20 events could deplete the outer belt. Similarly, Shekhar et al. (2020) used NOAA/POES satellites and BARREL to quantify the relativistic electron loss for 11 events on January 17, 2013. They estimate a net loss of 5% of the electrons with energies above 700 keV.

Thorne and Kennel (1971) suggested that Electromagnetic Ion Cyclotron (EMIC) waves can generate REP in the $E > 1$ MeV range, which would imply simultaneous observation of REP and increases in proton precipitation in the anisotropic proton zone where protons are unstable to wave growth. This correlation was observed by Søråas et al. (2005) using the Polar Operational Environmental Satellites (POES) by matching the proton flux increases observed by the P1 (52 keV differential proton flux) and relativistic electron increases observed by P6 (> 800 keV when used for electrons) channels. Sandanger et al. (2007, 2009) used the same channels to show that the proton and electron enhancements are consistent with scattering into the loss cone by EMIC waves. Carson et al. (2013) analyzed EMIC-driven REP using 12 years of POES observations and found that the majority of events occur in the pre-midnight and midnight sectors around $L \sim 5$. Other spacecraft such as the FIREBIRD-II cubesats observed electron precipitation in the 200-300 keV range while in conjunction with EMIC waves detected by the the Van Allen Probes,

suggesting that EMIC waves can efficiently scatter a wide energy range of electrons (Capannolo et al., 2021). REP has been also observed by the Balloon Array for Radiation belt Relativistic Electron Losses (BARREL) in conjunction to EMIC waves measured by a Geostationary Operational Environmental Satellite (GOES) spacecraft at dusk (Blum, Halford, et al., 2015), and at pre-midnight by Van Allen Probes (J. Zhang et al., 2016). However, EMIC-driven events account for only a portion of all the REP occurring in the midnight sector, as CSS also plays an important role scattering relativistic electrons in the current sheet (Smith et al., 2016; Shekhar et al., 2017; Capannolo et al., 2022).

The periodicities observed by low altitude orbit spacecraft can help to detect REP events and also to distinguish between radiation belt crossings, precipitation bands, or microbursts. They can be examined with spectrograms to investigate the time evolution of the REP (Nakamura et al., 1995). Kataoka et al. (2016) used four-month data from the CALorimetric Electron Telescope (CALET) on the International Space Station (ISS) to show that 5-20s (50 - 200 mHz) periodicities are frequently present during REP events. These periodicities have been regularly observed (Mursula et al., 2001; Jacobs, 2012), and they have been associated with nonlinear wave growth of EMIC-triggered emissions as proposed by several numerical simulations (Omura & Zhao, 2012; Shoji & Omura, 2013; Kubota et al., 2015).

The use of periodicity analysis is an alternative to other methods currently used for the identification of REP events. In general, automatic algorithms are more efficient than methods based on visual inspection of data, and are less sensitive to biases in the analysis of large amount of data (Bortnik et al., 2007). However, they are susceptible to noise-to-signal ratio problems inducing false positive cases if the detection threshold is reduced with the intention of identifying small amplitude events (Guralnik & Srivastava, 1999). Currently, microburst-detection algorithms have shown to be effective, but have not been equally efficient for the detection of precipitation bands (O'brien et al., 2003; Blum, Li, & Denton, 2015). We present here a novel method for automatic detection and analysis of REP.

1.1 The CALET Experiment

The CALET experiment was designed to observe high-energy cosmic rays and has been operational since October 2015. The instrument is attached to the Japanese Mod-

ule “Kibo” at the ISS and has the scientific objective to study high-energy phenomena of the Universe (Torii & Collaboration, 2007; Torii, 2016; Asaoka et al., 2018; Torii et al., 2019). The two scintillator arrays constituting the charge detector (CHDX and CHDY) at the top of the apparatus used to identify the incident cosmic rays charge are also sensitive to electrons with energies > 1.5 MeV and > 3.4 MeV, respectively (Bruno et al., 2022). This makes the CHDX, CHDY pair suitable for the detection of hard spectra REP events (Kataoka et al., 2016). This capability is particularly useful since CALET is one of the few instruments available at this energy range for conjugate MeV electrons studies during the Van Allen probes era (2012-2019). Its data have already been used for the study of the relation between some REP events and magnetospheric waves (Kataoka et al., 2020; Bruno et al., 2022).

The REP events observed by CALET are identified by isolated increases in count rates measured by the CHDX/CHDY detectors. Figure 1a shows several hours of data from November 10, 2015 where the peaks correspond to relativistic electrons. Figure 1b shows an example of a REP observation. They are characterized by rapid variations that can last from a few seconds to several minutes. In some cases, both types of profiles (smooth and rapid profiles) are present at the same time (see Figure 1c). Automated detection algorithms for these types of events can be more complex to design as they would also require a previous knowledge about the existence of each type of signature and their characteristics. Another class of events consists in smooth profiles mostly associated with protons detected in the South-Atlantic-Anomaly region and, similarly, electrons in the innermost part of the outer radiation belt ($L \sim 3$) (Kataoka et al., 2016, 2020; Bruno et al., 2022). Such events are identified as a gradual increase-then-decrease of the count rates with a timescale typically of 5-10 minutes. Figures 1e to g consist of the continuous wavelet transform (Aguiar-Conraria & Soares, 2014) of the observations showing the contrasting variability of the CHDX channel for smooth and rapid relativistic electrons profiles, respectively. It is important to mention that since REP events can last several hours and extend in latitude and longitude, the same REP event can be detected during consecutive orbits (Nakamura et al., 1995; Blake et al., 1996; Blum et al., 2013; Bruno et al., 2022).

The data used in this study have a continuous coverage from October 2015 to October 2021. The data has quasi-periodic sampling time resolution, with an average period of 1 second. The ISS (therefore CALET) is located at low Earth orbit (LEO) at 370-

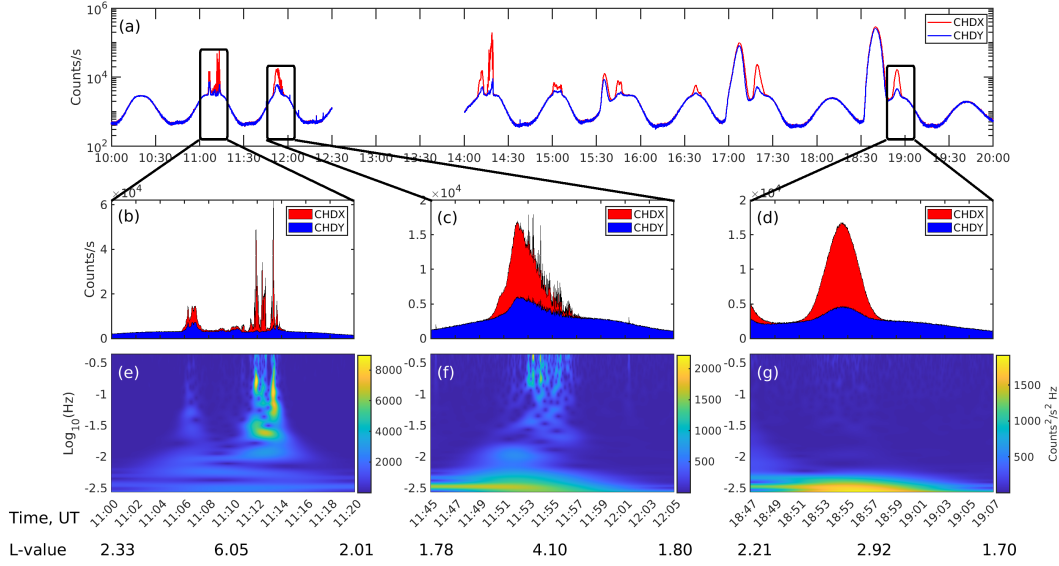


Figure 1. (a) Ten hours of CALET CHDX (red; $E > 1.5$ MeV) and CHDY (blue; $E > 3.4$ MeV) data in counts/s. The sharp spikes represent sudden increases of relativistic electrons. (b) Example of a rapid electron precipitation event. (c) Example of a combined smooth and rapid profiles of relativistic electrons. (d) Example of a smooth profile of relativistic electrons. (e) Continuous wavelet transform of the rapid electron precipitation event shown in plot b. (f) Continuous wavelet transform of combined event shown in plot c. (g) Continuous wavelet transform of a smooth profile of relativistic electrons event shown in d. Data gap is present between 12:30 and 14:00.

460 km of altitude and has an inclination of 51.6° . ~~As a result~~In consequence, the ISS visits $L=4-7$ regions several times a day at a similar magnetic local time (MLT) enabling periodic sampling of the outer radiation belt. The ISS exhibits a precession time of 60 days. This implies that the MLT at which the CALET probes the high L -shell also follows the same 60-day periodicity.

2 Methodology

A self-organizing-map (SOM) is an unsupervised machine learning technique used to define an ordered mapping, as a projection from a set of given data items onto a regular, usually two-dimensional grid of nodes. A data item will be mapped into the most similar node, based on the smallest distance from the node in some metric (Kohonen, 1982, 1990, 2013). The SOM technique has been widely used for unsupervised cluster-

ing of different kinds of data set in biology, chemistry, sociology, and economics (Akman et al., 2019; Mele & Crowley, 2008; Yang & Chou, 2003; Collan et al., 2007), but lately also for identification of magnetospheric regions (Innocenti et al., 2021) and categorization of plasma waves (Vech & Malaspina, 2021).

The SOM is a competitive learning neural network model. The neural network consists of a grid of nodes initially built from randomly selected samples in the data set. This means that identical results can theoretically only be guaranteed when the same seed is used during the pseudo-random selection of samples. However, converging results will generate mirrored, rotated, or identical maps. Since the distribution of the clusters with respect to each other in mirrored or rotated maps is the same, the interpretation of the map remains unchanged in these cases.

The learning process is based on an iterative search of the *best-matching-unit* (BMU) for each one of the samples in the data set. The BMU is the most similar unit (or node) to each value of the data set during each iteration. The similarity between the nodes and the data can be evaluated with multiple metrics; the most popular one, used in this study is the Euclidean distance $\left(d(q_i, p_i) = \sqrt{\sum (q_i - p_i)^2}\right)$ where q and p represent the current sample and current unit, respectively. During each iteration, the BMU and the nodes surrounding it are updated to become more similar to the latest input sample evaluated. The updates are made based in the learning rate ($\eta = \eta_0 e^{-t\lambda}$) that controls how much weight the last sample has on the update of the BMU. The radius of influence ($\sigma = \sigma_0 e^{-t\beta}$) determines the influence of the input vector in the surrounding clusters where t correspond to the current iteration and λ and β are the respective decay rates for the learning rate and the radius of influence, respectively. For both steps we used $\eta_0 = 0.1$, $\sigma_0 = \sqrt{2}$ and $\beta = 0.1$. The behavior of the SOM to these free parameters is standard to any SOM, they are initially defined defined by the size of the map and the similarity between the observations and later adjusted for better performance. Different parameters will determine how fast (i.e. after how many iterations) the map converges to a stable solution or if it does not converge at all. We tested multiple combinations of parameters and selected the above because they result in the map converging to the same result even when different seeds are used for the random selection of the initial map, which is evidence of a converging solution. In addition, as it will be shown below, we observed only a small number of incorrectly classified observations using these parameters.

Here we implement the SOM technique to classify the observations from CALET and analyze the precipitation patterns found. This process is performed in two steps: (1) detection of rapid electron precipitation observation events; (2) and classification of rapid precipitation observation events. The first step uses the Power-Spectral-Density (PSD) calculated from 10 minute windows of data as input for the SOM while the second step uses an interval-integrated-PSD. The details of the implementation of the SOM are explained in the following section [and a diagram of the methodology implemented can be found in the Supporting Information \(Figure S2\)](#).

The CALET data set is collected at a nearly constant rate of 1-second. The data is re-sampled to 1-second as uniform sampling is required for spectral analysis used in this study. The re-sampling helps to reduce aliasing and contributes to removing small data gaps. Windows with gaps larger than 3 seconds are discarded as they would introduce a spurious response during the application of the [Fast-Fourier-Transform](#) (FFT). The re-sampled data is subdivided into 10 minute windows starting from October 2015 until October 2021. This choice is based on the ISS orbital constraints, since REP events can be observed only for a few minutes during each pass. The SOM technique is applied two times for similar, but different objectives. In the first place, the SOM is applied with the objective of distinguishing rapid precipitation from the smooth profile intervals, and background noise. During this step, the SOM is implemented using the PSD of each one of the windows as input; the PSDs are calculated from the count rates of the CHD channels to capture the intrinsic variability of the observed relativistic electrons. In this step, the Euclidean distance is computed using the current event spectral power at each frequency (q_i) and the current node spectral power at each frequency (p_i). The PSD are calculated using the ~~Fast-Fourier-Transform~~ FFT with 100 ~~FFT~~ points, in order to compute the PSD while keeping a fast computational time. The number of FFT points should be increased if data with higher sampling resolution is used. The output is a map of clusters where every cluster contains a subset of PSD with shared similarities in overall power and power distribution in frequency. Exclusively focusing on REP events, we chose clusters with zero smooth profiles or background noise, effectively eliminating these elements from the analyzed sample. We are then left with a “cleaned” data set of only rapid precipitation observations for further study.

During the second step only rapid precipitation observations are considered. However, it is possible that more than one rapid precipitation event occurs during a 10 minute

interval. In order to separate multiple REP events in the same 10 minute interval, we apply a 60-second long moving window that computes the variance along the interval, and normalize such variance by dividing by its norm. Based on visual inspection we established a tolerance of 0.1 [counts/s]^2 to detect the beginning and ending of the rapid precipitation event. There are cases when two consecutive rapid precipitation observations occur in periods less than 10 minutes: this usually happens when the ISS crosses a region where relativistic precipitation is observed by CALET during the ascending and descending orbital passes. When these observations are separated, two time series of different lengths are generated. To obtain two same-length time series consistent with the rest of the data, the edges of the series are filled with generated background noise similar to that seen by CALET when only background particles are observed.

The lower limit on the PSDs are set to 100 mHz to remove the effects associated with the rapid movement of the ISS. The upper limit of the PSDs are set to 500 mHz since aliasing due to 1 second sampling rate should equally affect the detection of all very rapid precipitation observed. Since the SOM technique is most efficient with a low number of variables, we created an equivalent representation of the PSDs with a lower number of variables by dividing each PSD in 10 bins with 50% overlap and integrating the PSD each bin to obtain a simplified PSD profile. This procedure allows us to simplify the PSD and forces the SOM to classify by overall power of the PSD and power distribution in frequency.

Once all the events are individualized and standardized, we apply the k -means technique to calculate the number of clusters (k -value) that minimize total variances between all the events contained in each cluster. Finally, the SOM technique is applied to the interval-integrated-PSD of the rapid precipitation observations with the objective of classifying different features of the precipitation in order to identify different types of rapid precipitation events.

The output is a grid of clusters (or map) where each cluster consists of precipitation events with similar PSD characteristics. We examine the properties of the precipitation events in each cluster to explore their dependence on various variables and better determine the physical meaning behind the SOM's categorizations.

3 Results

3.1 First Step Results

The objective of the first step is to detect rapid precipitation observations without the need of extensive visual inspection of the data, or an algorithm that requires a detailed knowledge about the characteristics of the data. The SOM is able to not only identify isolated rapid precipitation intervals, but also events where smooth profiles and rapid precipitation occur simultaneously. In order to validate the SOM technique with CALET data, we visually inspected all the clusters to verify the observations were correctly classified. During the time period covered in this study, the SOM identified 1448 rapid precipitation events, 21301 intervals were classified as smooth profiles of relativistic electrons and the rest (275241) identified as background noise. We visually inspected all 1448 events classified by the SOM as rapid precipitation and found 87 events (6.0%) to be false positives (events incorrectly classified as rapid). We also performed a survey over half of the events that were classified as smooth profile events to quantify the number of false negatives. From a visual survey of 11545 events that were identified as smooth profile events, we found 27 false negatives or 0.23% of the events. The number of windows classified as noise is too large to be evaluated by visual inspection, so we randomly selected 5000 time windows classified by the SOM as noise for visual identification. Of this sample we found 9 false negatives, or 0.18% of the events. We performed a z-test to calculate a confidence interval and found the total number of false negatives in the background noise to be 495 ± 172 with a 95% of confidence.

As demonstrated by Figure 2a, the geographic distribution of smooth-profile events concentrates in the South-Atlantic-Anomaly region. Another component is present in the southern hemisphere around $L \sim 3$, corresponding to trapped and quasi-trapped (drift-loss-cone) electrons in the inner boundary of the outer radiation belt, where trapped electrons correspond to electrons that can stably drift around Earth unless perturbed, and quasi-trapped correspond to electrons that will bounce several times before precipitation occurs (Selesnick et al., 2003; Tu et al., 2010; Pham et al., 2017; K. Zhang et al., 2017). Meanwhile, the rapid profiles (Figure 2c) are typically detected at higher magnetic latitudes, mapping to the footprint of the outer radiation belt ($L \sim 4-6$).

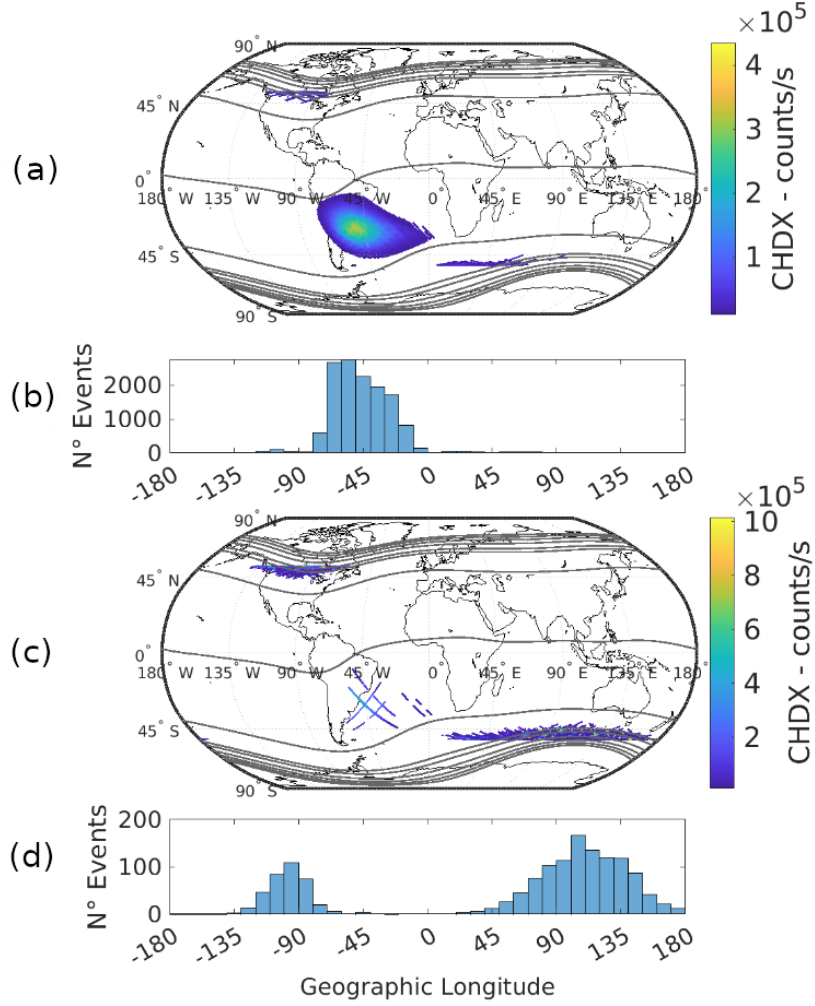


Figure 2. (a) Positions of the first 1000 smooth profiles as an example. (b) Geographic longitude histogram of all smooth profile events. (c) Positions of all REP events between October 2015 to October 2021. The color indicates the counts/s observed by CALET. L-shell curves from $L=1$ to $L=8$ in dark gray. (d) Geographic longitude histogram of all rapid events. Note that the latitude of CALET observations is constrained by the inclination of the ISS orbit (51.6°).

3.2 Second Step Results

The objective of the second step is to analyze the maps generated in step 2, consisting of only REP events to uncover patterns associated with the magnitude and variability of the REP events observed. The number of clusters is determined using the k -means (k being the number of clusters) technique (Likas et al., 2003). k -means acts as a classifier that minimizes the within-cluster variances given a predetermined number

of clusters. We found that the optimal number of clusters is 15 and to simplify the analysis the rapid precipitation observation events are classified into 16 clusters to keep the map square. With the objective to study the precipitation L-MLT patterns and the associated variability, we evaluate the clusters in terms of the frequency interval that carries the maximum power in the PSD, the energy spectra index, and the distance to the plasmapause of the observations.

The median frequency at which the PSD peaks considering all events is 183 mHz (T=5.5 seconds). Figure 3 shows the PSD of the classified clusters. Clusters 1-4 and 6-8, and 11 have most of their power above 183 mHz, while clusters 5, 9-10, and 12-16 are dominated by lower frequency signatures. Since each cluster is filled with individual PSDs corresponding to precipitation events, for each of them we calculate a median curve of the PSDs using the median value at each frequency. We also estimate the 25% and 75% curves to observe the distribution of the variability of the events at each frequency.

For each cluster four representative values are calculated for the events in the respective cluster: The median of the frequency at the PSD maximum amplitude of each PSD; the median of the maximum amplitude of each PSD; the median of the maximum spectral hardness; and the median of the distance to the plasmapause. The clusters are then sorted using each one of these values. We compare the group of clusters that show the maximum dissimilarity to enhance the characteristics that could be useful for analysis. We achieve this by comparing the clusters below the 25 and above 75 percentile, respectively of the four computed values that represent one characteristic of the clusters.

When comparing the representative frequency at the PSD maximum amplitude, the two groups show differences in their MLT and L-shell distributions. Since the distributions were close to a Gaussian, we performed the significance Z-test with a Z-value=5.86. Similarly, we use Monte Carlo test to compute the probability that such distribution difference can be due to randomness. The median difference between both distributions is larger than in 96.2% of random distributions computed. Both tests are performed with a 95% of confidence to estimate that the discrepancy between both distributions is statistically significant.

Figure 4 shows the distribution in [the mapmaps](#) of different characteristics of the clustered events. They demonstrate how other characteristics associated to the events distribute when the SOM organizes the events by their PSD. Figure 4a shows the result-

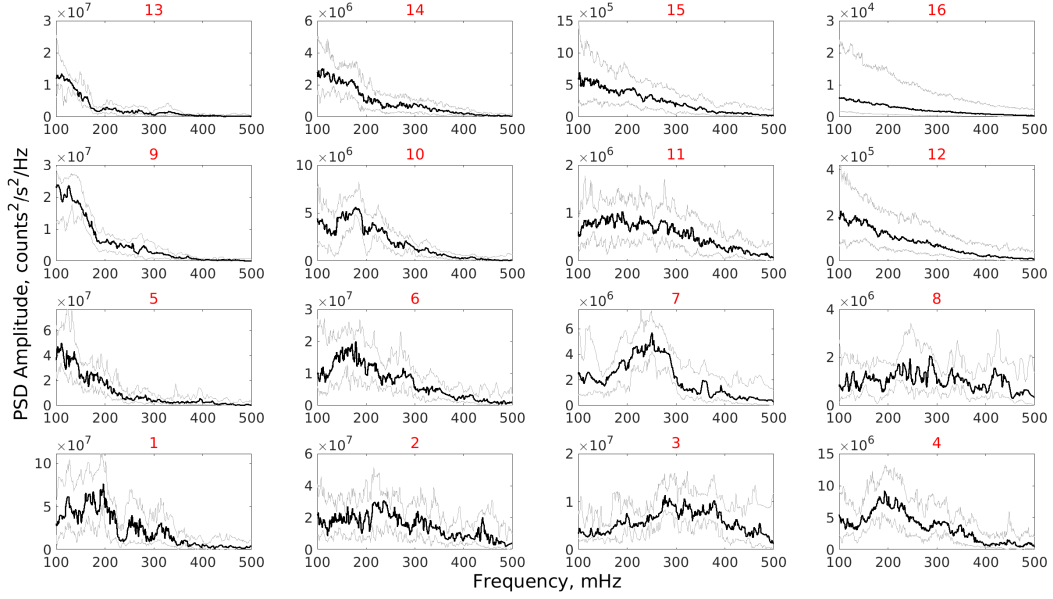


Figure 3. PSD of all clusters. The black curves represent the median of all the events of each cluster. Gray curves correspond to the 25 and 75 percentiles at each frequency of the PSD of the events in each cluster. Red numbers indicate the number of the respective cluster.

ing map where the colors indicate the median frequency in each cluster at which power spectral density peaks. The clusters where the dominant frequency is above 183 mHz contain events where high-frequency periodicity electron precipitation is dominant. Figure 4b displays the percentage of REP weighed by the total number of passes through every L-MLT grid cell, demonstrating that low-periodicity (below the 25 percentile) events are dominant at pre-midnight and between L=5-6. Figures 4c shows that high-periodicity (above the 75 percentile) events occur at local times, but are more likely to occur in the midnight sector between L=5-7.

Figure 4d displays the median value of the highest amplitude in the PSD for each cluster. We use again the clusters where the median frequency is below the 25th or above the 75th percentile to separate them into two groups. Figure 4e shows that small amplitude events occur predominantly at midnight. In the midnight sector they are observed at L=5-7. Finally, Figure 4f demonstrates that rapid precipitation with larger amplitudes is dominant in the pre-midnight sector and between L=5-6.

We also evaluate the event energy spectra in each cluster. We use the ratio between the count rates measured by the two sensors to calculate an energy spectral index (CHDX/CHDY).

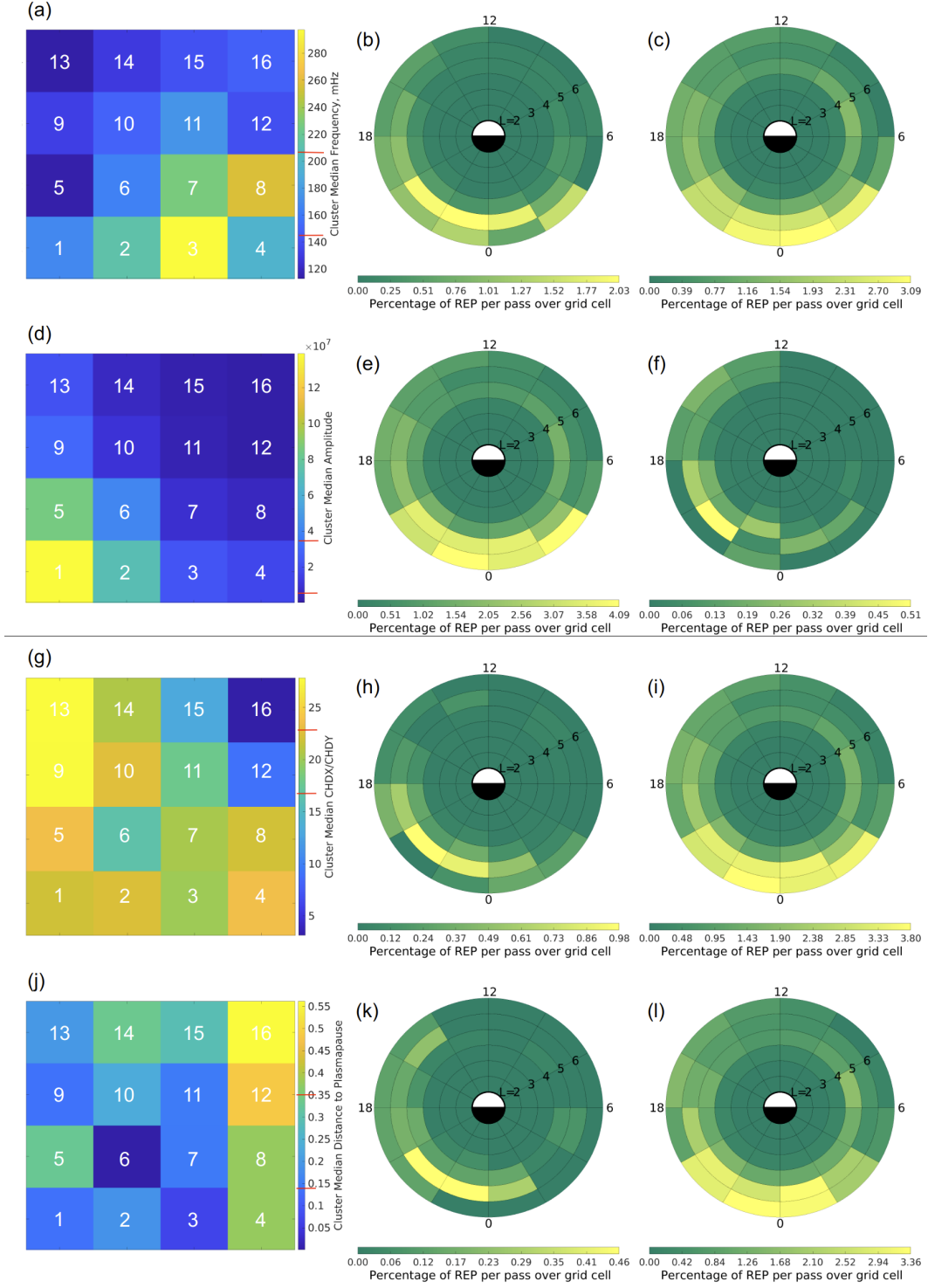


Figure 4. Left column: Maps of clusters. Middle column: Bivariate histogram of clusters under the 25 percentile. Right column: Bivariate histogram of clusters above the 75 percentile. (a-c) Median of the dominant periodicities. (d-f) Median of the PSD amplitude. (g-i) Median of the energy spectral index. (j-l) Median of the distance to the plasmopause. L-shell histograms can be found in the Supporting Information.

The energy spectral index was calculated using the maximum CHDX/CHDY ratio during the event. Since CHDX and CHDY detect electrons with energies above 1.5 and 3.4 MeV, respectively, larger values of the spectral index correspond to a softer spectrum associated with the precipitation. Figure 4g shows the same kind of map as Figures 4a and 4d, but with the color code denoting the median energy spectral index of each cluster. Figure 4h demonstrates that events from clusters with softer energy spectral index (CHDX/CHDY above 75th percentile) are concentrated in the pre-midnight sector and at $L = 5-6$. In contrast, Figure 4i shows that events from clusters with a harder energy spectral index (CHDX/CHDY below 25th percentile) are common at all MLT, but predominantly observed in the midnight sector at $L=5-7$.

Lastly, we calculate the location of the events with respect to the plasmopause. Moldwin et al. (2002) MLT-dependant empirical model has been used in numerous other studies to analyze the spatial distribution of waves (Carson et al., 2013; D. Wang et al., 2015; Saikin et al., 2016), and to investigate the location of the outer belt with respect to the plasmopause (X. Li et al., 2006) among other studies. We use this model to calculate the location of the plasmopause and estimate its distance to the REP detection location (ΔL) in order to see if different precipitation types exhibit any correlation by their distance to the plasmopause. Figure 4j shows the median ΔL of the events in each cluster. Figure 4k shows that the clusters with a median distance to the plasmopause below the 25th percentile are more common near the pre-midnight sector $L=5-6$. In contrast, the clusters with a median distance above the 75th percentile are more frequent in the pre-midnight and midnight sectors at $L=5-7$.

4 Discussion

The results presented in the previous sections suggest that the SOM is an efficient tool for separating different types of REP observations time series by classifying their PSD. It effectively distinguishes rapid precipitation events from smooth profiles, and background noise, eliminating the need for extensive visual inspection or the use of standard automated algorithms that are often sensitive to signal-to-noise ratio detection thresholds. The SOM is also capable of classifying rapid precipitation events by the periodicities and the power of the PSD. We use the median, in addition to 25 and 75 percentiles values of the dominant frequency, peak PSD amplitude, energy spectral index, and distance to plasmopause of the rapid precipitation as reference to separate the precipita-

tion into different populations. The results show that precipitation with different characteristics can generate similar precipitation patterns, demonstrating the classification of rapid precipitation is a multidimensional problem. They also reveal features through sorting based on PSD alone, allowing the identification of different precipitation components with varying properties.

Microbursts and precipitation bands are example of two types of REP with the periodicity of the electron fluxes among the observational characteristics that distinguish them. While whistler mode chorus waves are the primary mechanism believed to drive microbursts, electrostatic and EMIC waves are believed to drive precipitation bands (Thorne & Kennel, 1971; Blum, Li, & Denton, 2015). However, the observation of precipitation bands at conjugated locations and consecutive orbits (Blake et al., 1996), suggests that their characteristic signature is related to spatial rather than temporal characteristics (Lorentzen et al., 2001; Bortnik et al., 2006; Blum, Li, & Denton, 2015).

Carson et al. (2013); Z. Wang et al. (2014); Gasque et al. (2021) used an algorithm applied to POES P1 (52 keV differential proton flux) and P6 (>800 keV when used for electrons) channels to detect EMIC-driven REP events. These authors found that EMIC-driven REP are predominantly detected in the dusk-midnight sector around $L \sim 5$. The CSS mechanism also occurs in the midnight sector and it is sometimes even more efficient than wave-driven REP. While previous studies have associated REP near midnight to EMIC waves, it has been speculated that softer REP events are driven by CSS while harder precipitation events are more likely to be driven by EMIC waves (Smith et al., 2016; Shekhar et al., 2018; Capannolo et al., 2021). Capannolo et al. (2022) performed a conservative classification between EMIC-driven and CSS-driven REP events to ensure events were truly driven by one mechanism alone and found that near 40% of the classified events were CSS-driven.

The results of this analysis show similarities with the findings of aforementioned studies. For instance, Figures 4h and i show that REP events can be separated by their relative spectral hardness into at least two populations that overlap near midnight. Figure 4h shows that softer precipitation events mainly occur in the pre-midnight sector between $L=4-5$. Figure 4i shows that hard precipitation is observed at all MLT, but they are mainly localized in the midnight sector. Some events are seen in the morning sector where microbursts are commonly observed. However, the microburst variability (~ 100

ms) cannot be resolved by the 1 second time resolution of the CALET data set used in this work, making it hard to investigate the origin of these hard precipitation events.

The classification by variability also separates the REP observations into two populations. Kataoka et al. (2016) also studied periodicities observed by CALET in the dusk and pre-midnight sector finding similar periodicities that have been associated to non-linear wave growth of EMIC-triggered emissions by several numerical simulations and observational studies. The REP events with low variability are more frequent in the pre-midnight sector where EMIC-driven precipitation is more commonly observed. On the other hand, REP events with higher variability are more frequently observed in the midnight sector near where CSS-driven precipitation is more frequent. The morphology of the REP patterns and their similarity to EMIC-driven REP and CSS-driven REP patterns reported by Yahnin et al. (2016) suggests a potential connection between the variability observed and the driver of the precipitation. Low variability REP are more common in the same region where EMIC-driven REP are often observed. Meanwhile, high variability REP are observed where CSS-driven REP are most commonly observed.

In all cases, an L-MLT pattern with a predominant occurrence of events in the pre-midnight sector has been generated, similar to the one observed for EMIC-driven REP. However, the REP classification cannot be directly associated with drivers without conjugated observations. Typically, EMIC-driven REP and CSS-driven REP have been difficult to distinguish from each other as they often can occur simultaneously, and currently only a small portion of the observations can be truly classified as EMIC or CSS-driven precipitation (Capannolo et al., 2022).

The results of this work demonstrate that there is information about REP hidden in the variability of the observations that can be used for future studies to distinguish and analyze their drivers.

5 Conclusions

In this study, we have described a new use of an unsupervised machine learning technique to classify time series of relativistic electron precipitation. We have tested the capabilities of SOM for the analysis of the rapid relativistic electron precipitation observed by CALET in the 2015-2021 period. The SOM has automatically detected rapid electron precipitation intervals and classified them by the main characteristics of their PSD.

It has been shown that the SOM technique is a robust method for event detection. The SOM is capable of detecting rapid electron precipitation events of any magnitude, even if they are superposed with smooth profiles. The SOM has also been implemented to classify the rapid precipitation observations. The output of the maps suggests that the SOM technique can categorize rapid precipitation into different types of precipitation with different properties.

The energy spectral index and distance to the plasmapause exhibit a similar L-MLT pattern than the one obtained for periodicities and amplitude, but when different clusters are grouped. This is most likely due to the existence of multiple high and low periodicities for rapid precipitation, such as microbursts and precipitation bands that have different L-MLT distributions. This also reveals the complexities of REP analysis as multiple precipitation types, with different characteristics, may have similar patterns in L-MLT. It also shows that unsupervised machine learning is a useful tool for disentangling this multidimensional problem.

We have demonstrated that this technique has the potential for the identification of electron precipitation in LEO observations, and to distinguish different types of precipitation. As next steps, we plan to use it in conjugated studies between CALET and the Van Allen Probes that would help to determine the specific common characteristics of rapid precipitation observations in each one of the clusters obtained from the SOM.

6 Data Availability Statement

The CALET data used in this study are publicly available (`data.darts.isas.jaxa.jp/pub/calet/cal-v1.1/CHD/level1.1/obs/`) in ASCII format in the Data ARchives and Transmission System (DARTS) of the Japan Aerospace Exploration Agency (JAXA). The catalog of REP observation events is attached in a text file. The Supporting Information contains a description of the catalog and necessary considerations when using the catalog.

Acknowledgments

The authors acknowledge the support of this study by NASA/Living With a Star Science program NNH20ZDA001N-LWS and NASA's H-SR award 80NSSC21K1682 as well as by NASA 80NSSC20K0397 at Louisiana State University and NNH18ZDA001N-APRA18-

004 at Goddard Space Flight Center. We would also like to thank the CALET collaboration team. The authors also acknowledge the input of the reviewers which contributed to improve the quality of this article.

References

- Aguiar-Conraria, L., & Soares, M. J. (2014). The continuous wavelet transform: Moving beyond uni-and bivariate analysis. *Journal of Economic Surveys*, 28(2), 344–375.
- Akman, O., Comar, T., Hrozencik, D., & Gonzales, J. (2019). Data clustering and self-organizing maps in biology. In *Algebraic and combinatorial computational biology* (pp. 351–374). Elsevier.
- Asaoka, Y., Ozawa, S., Torii, S., Adriani, O., Akaike, Y., Asano, K., . . . others (2018). On-orbit operations and offline data processing of calet onboard the iss. *Astroparticle Physics*, 100, 29–37.
- Blake, J., Looper, M., Baker, D., Nakamura, R., Klecker, B., & Hovestadt, D. (1996). New high temporal and spatial resolution measurements by sampex of the precipitation of relativistic electrons. *Advances in Space Research*, 18(8), 171–186.
- Blum, L., & Breneman, A. (2020). Observations of radiation belt losses due to cyclotron wave-particle interactions. In *The dynamic loss of earth’s radiation belts* (pp. 49–98). Elsevier.
- Blum, L., Halford, A., Millan, R., Bonnell, J., Goldstein, J., Usanova, M., . . . others (2015). Observations of coincident emic wave activity and duskside energetic electron precipitation on 18–19 january 2013. *Geophysical Research Letters*, 42(14), 5727–5735.
- Blum, L., Li, X., & Denton, M. (2015). Rapid mev electron precipitation as observed by sampex/hilt during high-speed stream-driven storms. *Journal of Geophysical Research: Space Physics*, 120(5), 3783–3794.
- Blum, L., Schiller, Q., Li, X., Millan, R., Halford, A., & Woodger, L. (2013). New conjunctive cubesat and balloon measurements to quantify rapid energetic electron precipitation. *Geophysical research letters*, 40(22), 5833–5837.
- Bortnik, J., Cutler, J., Dunson, C., & Bleier, T. (2007). An automatic wave detection algorithm applied to pc1 pulsations. *Journal of Geophysical Research:*

- 530 *Space Physics*, 112(A4).
- 531 Bortnik, J., Thorne, R., O'Brien, T., Green, J., Strangeway, R., Shprits, Y., &
 532 Baker, D. (2006). Observation of two distinct, rapid loss mechanisms during
 533 the 20 november 2003 radiation belt dropout event. *Journal of Geophysical*
 534 *Research: Space Physics*, 111(A12).
- 535 Bruno, A., Blum, L., de Nolfo, G., Kataoka, R., Torii, S., Greeley, A., ... Nakahira,
 536 S. (2022). Emic-wave driven electron precipitation observed by calet
 537 on the international space station. *Geophysical Research Letters*, 49(6),
 538 e2021GL097529.
- 539 Capannolo, L., Li, W., Millan, R., Smith, D., Sivadas, N., Sample, J., & Shekhar,
 540 S. (2022). Relativistic electron precipitation near midnight: Drivers, distribu-
 541 tion, and properties. *Journal of Geophysical Research: Space Physics*, 127(1),
 542 e2021JA030111.
- 543 Capannolo, L., Li, W., Spence, H., Johnson, A., Shumko, M., Sample, J., &
 544 Klumpar, D. (2021). Energetic electron precipitation observed by firebird-
 545 ii potentially driven by emic waves: Location, extent, and energy range from a
 546 multievent analysis. *Geophysical Research Letters*, 48(5), e2020GL091564.
- 547 Carson, B. R., Rodger, C. J., & Clilverd, M. A. (2013). Poes satellite observations
 548 of emic-wave driven relativistic electron precipitation during 1998–2010. *Jour-*
 549 *nal of Geophysical Research: Space Physics*, 118(1), 232–243.
- 550 Collan, M., Eklund, T., & Back, B. (2007). Using the self-organizing map to visual-
 551 ize and explore socio-economic development. *Ebs Review*, 22(1), 6–15.
- 552 Crew, A. B., Spence, H. E., Blake, J. B., Klumpar, D. M., Larsen, B. A., O'Brien,
 553 T. P., ... others (2016). First multipoint in situ observations of electron mi-
 554 crobursts: Initial results from the nsf firebird ii mission. *Journal of Geophysical*
 555 *Research: Space Physics*, 121(6), 5272–5283.
- 556 Dachev, T. P. (2018). Relativistic electron precipitation bands in the outside ra-
 557 diation environment of the international space station. *Journal of Atmospheric*
 558 *and Solar-Terrestrial Physics*, 177, 247–256.
- 559 Gasque, L. C., Millan, R. M., & Shekhar, S. (2021). Statistically determining
 560 the spatial extent of relativistic electron precipitation events using 2-s polar-
 561 orbiting satellite data. *Journal of Geophysical Research: Space Physics*,
 562 126(4), e2020JA028675.

- 563 Guralnik, V., & Srivastava, J. (1999). Event detection from time series data. In
564 *Proceedings of the fifth acm sigkdd international conference on knowledge dis-*
565 *covery and data mining* (pp. 33–42).
- 566 Innocenti, M. E., Amaya, J., Raeder, J., Dupuis, R., Ferdousi, B., & Lapenta, G.
567 (2021). Unsupervised classification of simulated magnetospheric regions. In
568 *Annales geophysicae* (Vol. 39, pp. 861–881).
- 569 Jacobs, J. A. (2012). *Geomagnetic micropulsations* (Vol. 1). Springer Science &
570 Business Media.
- 571 Kataoka, R., Asaoka, Y., Torii, S., Nakahira, S., Ueno, H., Miyake, S., ... others
572 (2020). Plasma waves causing relativistic electron precipitation events at inter-
573 national space station: Lessons from conjunction observations with arase satel-
574 lite. *Journal of Geophysical Research: Space Physics*, 125(9), e2020JA027875.
- 575 Kataoka, R., Asaoka, Y., Torii, S., Terasawa, T., Ozawa, S., Tamura, T., ... Mori,
576 M. (2016). Relativistic electron precipitation at international space station:
577 Space weather monitoring by calorimetric electron telescope. *Geophysical*
578 *Research Letters*, 43(9), 4119–4125.
- 579 Kohonen, T. (1982). Self-organized formation of topologically correct feature maps.
580 *Biological cybernetics*, 43(1), 59–69.
- 581 Kohonen, T. (1990). The self-organizing map. *Proceedings of the IEEE*, 78(9),
582 1464–1480.
- 583 Kohonen, T. (2013). Essentials of the self-organizing map. *Neural networks*, 37, 52–
584 65.
- 585 Kubota, Y., Omura, Y., & Summers, D. (2015). Relativistic electron precipita-
586 tion induced by emic-triggered emissions in a dipole magnetosphere. *Journal of*
587 *Geophysical Research: Space Physics*, 120(6), 4384–4399.
- 588 Li, W., & Hudson, M. (2019). Earth’s van allen radiation belts: From discovery
589 to the van allen probes era. *Journal of Geophysical Research: Space Physics*,
590 124(11), 8319–8351.
- 591 Li, X., Baker, D., O’Brien, T., Xie, L., & Zong, Q. (2006). Correlation between the
592 inner edge of outer radiation belt electrons and the innermost plasmopause
593 location. *Geophysical research letters*, 33(14).
- 594 Likas, A., Vlassis, N., & Verbeek, J. J. (2003). The global k-means clustering algo-
595 rithm. *Pattern recognition*, 36(2), 451–461.

- 596 Lorentzen, K., Blake, J., Inan, U., & Bortnik, J. (2001). Observations of relativistic
597 electron microbursts in association with vlf chorus. *Journal of Geophysical Re-*
598 *search: Space Physics*, 106(A4), 6017–6027.
- 599 Loto’Aniu, T., Thorne, R. M., Fraser, B., & Summers, D. (2006). Estimating
600 relativistic electron pitch angle scattering rates using properties of the electro-
601 magnetic ion cyclotron wave spectrum. *Journal of Geophysical Research: Space*
602 *Physics*, 111(A4).
- 603 Mele, P. M., & Crowley, D. E. (2008). Application of self-organizing maps for as-
604 sessing soil biological quality. *Agriculture, Ecosystems & Environment*, 126(3-
605 4), 139–152.
- 606 Millan, R., & Thorne, R. (2007). Review of radiation belt relativistic electron losses.
607 *Journal of Atmospheric and Solar-Terrestrial Physics*, 69(3), 362–377.
- 608 Moldwin, M. B., Downward, L., Rassoul, H., Amin, R., & Anderson, R. (2002). A
609 new model of the location of the plasmopause: Crres results. *Journal of Geo-*
610 *physical Research: Space Physics*, 107(A11), SMP–2.
- 611 Mursula, K., Bräysy, T., Niskala, K., & Russell, C. (2001). Pc1 pearls revisited:
612 Structured electromagnetic ion cyclotron waves on polar satellite and on
613 ground. *Journal of Geophysical Research: Space Physics*, 106(A12), 29543–
614 29553.
- 615 Nakamura, R., Baker, D., Blake, J., Kanekal, S., Klecker, B., & Hovestadt, D.
616 (1995). Relativistic electron precipitation enhancements near the outer edge of
617 the radiation belt. *Geophysical research letters*, 22(9), 1129–1132.
- 618 O’Brien, T., Lorentzen, K., Mann, I., Meredith, N., Blake, J., Fennell, J., ... An-
619 derson, R. (2003). Energization of relativistic electrons in the presence of
620 ulf power and mev microbursts: Evidence for dual ulf and vlf acceleration.
621 *Journal of Geophysical Research: Space Physics*, 108(A8).
- 622 Omura, Y., & Zhao, Q. (2012). Nonlinear pitch angle scattering of relativistic elec-
623 trons by emic waves in the inner magnetosphere. *Journal of Geophysical Re-*
624 *search: Space Physics*, 117(A8).
- 625 Pham, K. H., Tu, W., & Xiang, Z. (2017). Quantifying the precipitation loss of ra-
626 diation belt electrons during a rapid dropout event. *Journal of Geophysical Re-*
627 *search: Space Physics*, 122(10), 10–287.
- 628 RA, G., FA, H., Kanekal, S., & PA, T. (1995). Mesospheric heating during highly

- relativistic electron precipitation events. *Journal of geomagnetism and geoelectricity*, 47(11), 1237–1247.
- Saikin, A., Zhang, J.-C., Smith, C., Spence, H., Torbert, R., & Kletzing, C. (2016). The dependence on geomagnetic conditions and solar wind dynamic pressure of the spatial distributions of emic waves observed by the van allen probes. *Journal of Geophysical Research: Space Physics*, 121(5), 4362–4377.
- Sandanger, M., Søråas, F., Aarsnes, K., Oksavik, K., & Evans, D. (2007). Loss of relativistic electrons: Evidence for pitch angle scattering by electromagnetic ion cyclotron waves excited by unstable ring current protons. *Journal of Geophysical Research: Space Physics*, 112(A12).
- Sandanger, M., Søråas, F., Sørbø, M., Aarsnes, K., Oksavik, K., & Evans, D. (2009). Relativistic electron losses related to emic waves during cir and cme storms. *Journal of Atmospheric and Solar-Terrestrial Physics*, 71(10-11), 1126–1144.
- Selesnick, R., Blake, J., & Mewaldt, R. (2003). Atmospheric losses of radiation belt electrons. *Journal of Geophysical Research: Space Physics*, 108(A12).
- Sergeev, V., Sazhina, E., Tsyganenko, N., Lundblad, J., & Søråas, F. (1983). Pitch-angle scattering of energetic protons in the magnetotail current sheet as the dominant source of their isotropic precipitation into the nightside ionosphere. *Planetary and Space Science*, 31(10), 1147–1155.
- Sergeev, V., & Tsyganenko, N. (1982). Energetic particle losses and trapping boundaries as deduced from calculations with a realistic magnetic field model. *Planetary and Space Science*, 30(10), 999–1006.
- Shekhar, S., Millan, R., & Hudson, M. (2018). A statistical study of spatial variation of relativistic electron precipitation energy spectra with polar operational environmental satellites. *Journal of Geophysical Research: Space Physics*, 123(5), 3349–3359.
- Shekhar, S., Millan, R., & Smith, D. (2017). A statistical study of the spatial extent of relativistic electron precipitation with polar orbiting environmental satellites. *Journal of Geophysical Research: Space Physics*, 122(11), 11–274.
- Shekhar, S., Millan, R., Woodger, L., & Qin, M. (2020). Quantification of the atmospheric relativistic electron precipitation on 17 january 2013. *Journal of Geophysical Research: Space Physics*, 125(9), e2020JA028014.
- Shoji, M., & Omura, Y. (2013). Triggering process of electromagnetic ion cyclotron

- 662 rising tone emissions in the inner magnetosphere. *Journal of Geophysical Re-*
 663 *search: Space Physics*, 118(9), 5553–5561.
- 664 Shprits, Y., Li, W., & Thorne, R. (2006). Controlling effect of the pitch angle scat-
 665 tering rates near the edge of the loss cone on electron lifetimes. *Journal of*
 666 *Geophysical Research: Space Physics*, 111(A12).
- 667 Shumko, M., Sample, J., Johnson, A., Blake, B., Crew, A., Spence, H., ... Handley,
 668 M. (2018). Microburst scale size derived from multiple bounces of a microburst
 669 simultaneously observed with the firebird-ii cubesats. *Geophysical Research*
 670 *Letters*, 45(17), 8811–8818.
- 671 Smith, D. M., Casavant, E. P., Comess, M. D., Liang, X., Bowers, G. S., Selesnick,
 672 R. S., ... Sample, J. G. (2016). The causes of the hardest electron precipita-
 673 tion events seen with sampex. *Journal of Geophysical Research: Space Physics*,
 674 121(9), 8600–8613.
- 675 Søråas, F., Aarsnes, K., Carlsen, D., Oksavik, K., & Evans, D. (2005). Ring cur-
 676 rent behavior as revealed by energetic proton precipitation. *The Inner Magne-*
 677 *tosphere: Physics and Modeling*, 155, 237–247.
- 678 Summers, D., & Thorne, R. M. (2003). Relativistic electron pitch-angle scattering
 679 by electromagnetic ion cyclotron waves during geomagnetic storms. *Journal of*
 680 *Geophysical Research: Space Physics*, 108(A4).
- 681 Thorne, R. M., & Kennel, C. (1971). Relativistic electron precipitation during mag-
 682 netic storm main phase. *Journal of Geophysical research*, 76(19), 4446–4453.
- 683 Torii, S. (2016). The calorimetric electron telescope (calet): a high-energy astropar-
 684 ticle physics observatory on the international space stati. In *The 34th interna-*
 685 *tional cosmic ray conference* (Vol. 236, p. 581).
- 686 Torii, S., & Collaboration, C. (2007). The calet experiment on iss. *Nuclear Physics*
 687 *B-Proceedings Supplements*, 166, 43–49.
- 688 Torii, S., Marrocchesi, P. S., & Collaboration, C. (2019). The calorimetric elec-
 689 tron telescope (calet) on the international space station. *Advances in Space Re-*
 690 *search*, 64(12), 2531–2537.
- 691 Tu, W., Selesnick, R., Li, X., & Looper, M. (2010). Quantification of the precipita-
 692 tion loss of radiation belt electrons observed by sampex. *Journal of Geophysi-*
 693 *cal Research: Space Physics*, 115(A7).
- 694 Ueno, H., Nakahira, S., Kataoka, R., Asaoka, Y., Torii, S., Ozawa, S., ... others

- 695 (2020). Radiation dose during relativistic electron precipitation events at the
 696 international space station. *Space Weather*, 18(7), e2019SW002280.
- 697 Vech, D., & Malaspina, D. M. (2021). A novel machine learning technique to iden-
 698 tify and categorize plasma waves in spacecraft measurements. *Journal of Geo-
 699 physical Research: Space Physics*, 126(9), e2021JA029567.
- 700 Wang, D., Yuan, Z., Yu, X., Deng, X., Zhou, M., Huang, S., ... others (2015). Sta-
 701 tistical characteristics of emic waves: Van allen probe observations. *Journal of
 702 Geophysical Research: Space Physics*, 120(6), 4400–4408.
- 703 Wang, Z., Yuan, Z., Li, M., Li, H., Wang, D., Li, H., ... Qiao, Z. (2014). Statistical
 704 characteristics of emic wave-driven relativistic electron precipitation with ob-
 705 servations of poes satellites: Revisit. *Journal of Geophysical Research: Space
 706 Physics*, 119(7), 5509–5519.
- 707 Xu, W., Marshall, R. A., & Tobiska, W. K. (2021). A method for calculating at-
 708 mospheric radiation produced by relativistic electron precipitation. *Space
 709 Weather*, 19(12), e2021SW002735.
- 710 Yahnin, A., Yahnina, T., Semenova, N., Gvozdevsky, B., & Pashin, A. (2016). Rela-
 711 tivistic electron precipitation as seen by noaa poes. *Journal of Geophysical Re-
 712 search: Space Physics*, 121(9), 8286–8299.
- 713 Yang, Z. R., & Chou, K.-C. (2003). Mining biological data using self-organizing
 714 map. *Journal of chemical information and computer sciences*, 43(6), 1748–
 715 1753.
- 716 Zhang, J., Halford, A. J., Saikin, A. A., Huang, C.-L., Spence, H. E., Larsen, B. A.,
 717 ... others (2016). Emic waves and associated relativistic electron precipita-
 718 tion on 25–26 january 2013. *Journal of Geophysical Research: Space Physics*,
 719 121(11), 11–086.
- 720 Zhang, K., Li, X., Schiller, Q., Gerhardt, D., Zhao, H., & Millan, R. (2017). De-
 721 tailed characteristics of radiation belt electrons revealed by csswe/reptile
 722 measurements: Geomagnetic activity response and precipitation observation.
 723 *Journal of Geophysical Research: Space Physics*, 122(8), 8434–8445.